Title
Structural Basis for Metastability in Amorphous Calcium Barium Carbonate (ACBC)

Journal
Advanced Functional Materials, 28(2)

ISSN
1616-301X

Authors
Whittaker, Michael L
Sun, Wenhao
DeRocher, Karen A
et al.

Publication Date
2018

DOI
10.1002/adfm.201704202

Peer reviewed

Structural Basis for Metastability in Amorphous Calcium Barium Carbonate (ACBC)

Michael L. Whittaker, Wenhao Sun, Karen A. DeRocher, Saivenkataraman Jayaraman, Gerbrand Ceder, and Derk Joester*

M. L. Whittaker, K. A. DeRocher, Prof. D. Joester Department of Materials Science and Engineering Northwestern University 2220 Campus Dr. Evanston, Evanston, IL 60208, USA E-mail: d-joester@northwestern.edu

Dr. W. Sun, Prof. G. Ceder Lawrence Berkeley National Laboratory Building 33, Berkeley, CA 94720, USA

S. Jayaraman Department of Materials Science and Engineering Massachusetts Institute of Technology Cambridge, MA 02139, USA

Abstract

Metastable amorphous precursors are emerging as valuable intermediates for the synthesis of materials with compositions and structures far from equilibrium. Recently, it was found that amorphous calcium barium carbonate (ACBC) can be converted into highly barium-substituted “balcite,” a metastable high temperature modification of calcite with exceptional hardness. A systematic analysis ACBC ($Ca_{1-x}Ba_xCO_3 \cdot 1.2H_2O$) in the range from x = 0–0.5 is presented. Combining techniques that independently probe the local environment from the perspective of calcium, barium, and carbonate ions, with total X-ray scattering and a new molecular dynamics/density functional theory simulations approach, provides a holistic picture of ACBC structure as a function of composition. With increasing barium content, ACBC becomes more ordered at short and medium range, and increasingly similar to crystalline balcite, without developing long-range order. This is not accompanied by a change in the water content and does not carry a significant energy penalty, but is associated with differences in cation coordination resulting from changing carbonate anion orientation. Therefore, the local order imprinted in ACBC may increasingly lower the kinetic barrier to subsequent transformations as it becomes more pronounced. This pathway offers clues to the design of metastable materials by tuning coordination numbers in the amorphous solid state.

1 Introduction

Carbonate mineralization is at the heart of many natural processes, including biomineralization and geological inorganic carbon cycling.[1] Crystalline carbonates are often preceded by amorphous precursors[2] that can have a strong influence on phase transformations and the structure and properties of the resulting crystals.[3] For example, it has been suggested that ACC occurs in several polyamorphs, which transform preferentially into the crystalline polymorph with the closest similarity in short-range order.[4-7] Similarly, balcite, a metastable, barium-substituted analog of high-temperature calcite with very high hardness, seems to be accessible only through an amorphous calcium–barium carbonate (ACBC) precursor with

similar short-range order.[8] Local order “imprinted” in the precursor is implicated in polymorph selectivity of subsequent phase transformations in these systems. Analogously, the local order of amorphous copper zinc carbonates is imprinted in copper–zinc oxide catalysts synthesized from them, which greatly enhances catalytic activity and lifetime compared to crystalline precursors.[9] Thus, local order established in diverse amorphous carbonate precursor phases may be utilized to access compositions and structures that are difficult to synthesize directly.[10] As polyamorphism is a common phenomenon in, for example, glasses of silica, ice, and metals, a deeper understanding of the interdependence of composition, structure, energetics, and crystallization pathways in (poly)amorphous structures is clearly needed.[11-13]

A significant factor affecting the lifetime of amorphous carbonates appears to be the ionic radius of the cation. While those with cations smaller than Ca^{2+}, including Mg^{2+}, Fe^{2+}, and Mn^{2+}, have been synthesized as bulk powders,[9, 14-18] those of larger cations, such as $Sr^{2+}$and Ba^{2+}, have not been observed in the absence of stabilizing additives[19-21] or in confinement[22] (with the notable exception of amorphous $RaCO_3$).[23] Structural water is thought to play an important role in controlling the lifetime and phase transformation rates of amorphous carbonates.[24-26] However, the impact of chemical composition or water content on amorphous carbonate structure remains poorly understood. To move toward a predictive theory of crystallization that accounts for metastable intermediates, it is therefore critical to elucidate the structural characteristics with the strongest influence over transformation rates in amorphous materials.[27]

In this work, we describe the synthesis and structure of metastable but long-lived ACBC ($Ca_{1-x}Ba_xCO_3{\cdot}1.2H_2O$). Using experimental techniques that interrogate the structure from the perspective of the cations (X-ray absorption spectroscopy at both calcium and barium K-edges), the anions (Raman and IR spectroscopy), and all atoms (electron diffraction, X-ray scattering, and pair distribution function analysis), we thoroughly characterize the short- (<5 Å) and mid-range (<15 Å) structure of ACBC. A combined molecular dynamics/density functional theory (MD/DFT) approach was utilized to connect structural motifs to thermodynamic properties. These analyses establish the importance of coordination geometry and carbonate orientation on the thermodynamics of amorphous carbonates, and help elucidate transformation pathways between metastable phases in this under-explored system.

2 Results

2.1 Synthesis and Stability

We synthesized ACBC ($Ca_{1-x}Ba_xCO_3{\cdot}1.2H_2O$) over a range of compositions. Briefly, ice cold aqueous solutions of alkaline earth chloride(s) with a total cation concentration of 1 M and a barium cation fraction x^{feed} (see Experimental Section) were rapidly mixed with equal volumes of ice cold

aqueous 1 M sodium carbonate. The resulting precipitate was filtered after 30 s, washed with water at 10 °C, and dried at reduced pressure (6.67 kPa) at ambient temperature for 24 h. Approximately 86% of the barium in solution is incorporated into ACBC (Table S1, Supporting Information).[8]

Synchrotron-based X-ray total scattering confirmed that the precipitates were amorphous up to $x = 0.55$ (Figure 1a). Left in its mother liquor for 24 h, ACBC crystallized at all compositions (Figure 1b). The presence of balcite in the crystallization products was confirmed by the shift of the most-intense calcite (104) peak to lower Bragg angle (larger *d*-spacing) and the gradual disappearance of the (113) with increasing barium. Only balcite was obtained between $x^{feed} = 0.25–0.56$. Between $x^{feed} = 0–0.25$, vaterite was found as secondary phase, while above $x^{feed} = 0.56$ witherite was also present. The composition of individual balcite particles was measured by energy dispersive spectroscopy (Table S1, Supporting Information). Balcite was enriched with barium relative to ACBC when vaterite was present, and depleted as the barium content in ACBC increased.

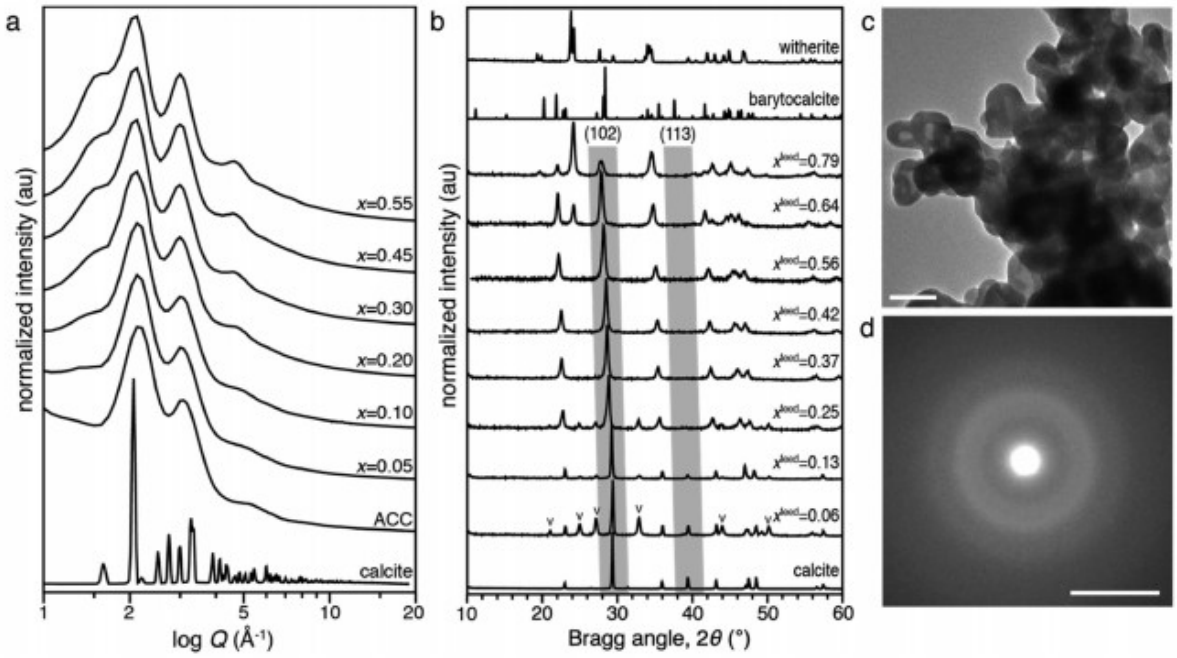

Figure 1

Characterization of ACBC precipitates. a) Synchrotron X-ray total scattering of ACBC compared to ACC and calcite. b) Products of the crystallization of ACBC at various concentrations of barium in the feed solution (x^{feed}) compared to crystalline reference compounds calcite ($CaCO_3$), barytocalcite ($Ca_{0.5}Ba_{0.5}CO_3$) and witherite ($BaCO_3$) by X-ray diffraction. Balcite is the primary crystalline phase for all compositions below $x^{feed} = 0.64$. Vaterite ("v," $CaCO_3$) was also present below $x^{feed} = 0.25$ as a minor phase impurity. c) TEM image of ACBC with $x = 0.51$, with d) SAED. Scale bar represents c) 100 nm or d) 5 nm^{-1}.

Thermal analysis was conducted immediately following ACBC synthesis to determine the amount of residual water and examine crystallization at elevated temperatures. Thermogravimetric analysis (TGA) indicated that

ACBC contained, on average, $n = 1.2 \pm 0.2$ formula units of water (Figure S1, Supporting Information). Similar amounts of water were found using ammonium carbonate instead of sodium carbonate, and at lower ion concentrations (Supporting Information). There was no correlation between the barium cation fraction, x, and total water content. Differential scanning calorimetry (DSC), acquired separately, in good agreement with simultaneous differential thermal analysis (DTA), was used to identify crystallization exotherms (Figure S2, Supporting Information). The temperature at which a crystallization exotherm first appeared in DTA and DSC increased with increasing barium (Table S2, Supporting Information).

2.2 Vibrational Spectroscopy

Raman spectra of ACBC samples with $x \leq 0.55$ were qualitatively similar to those of ACC (Figure 2a,b; Figures S3 and S4 and Table S3, Supporting Information). There were, however, systematic changes in the peak position and full width half maximum (FWHM) of several modes with increasing barium content. Line shapes of the most intense feature in Raman spectra, the ν_1 mode (symmetric carbonate stretch), were broad and Gaussian, in contrast to the narrow Voigt profiles of calcite and witherite. The ν_1 mode shifted to lower wavenumber, i.e., toward its position in witherite, and the full width-half maximum (FWHM) decreased with increasing barium content (Figure S4, Supporting Information). The much weaker ν_4 mode (in-plane bending, Figure S4, Supporting Information) was split in two, and was also considerably broadened compared to crystalline reference materials. Structural water and/or OH groups in both ACC and ACBC were confirmed by a characteristic broad band in the range ≈2800–3700 cm^{-1} (O–H stretch) and a very weak, broad band in the range of 1600–1700 cm^{-1} (H–O–H bending, Figures S3–S5, Supporting Information). IR spectra contain complementary information, and are discussed in detail the Supporting Information. When ACBC with $x = 0.41$ was dried under vacuum at elevated temperature (6.67 kPa, 50 °C, 8 h), the intensity of the O–H band between ≈2800–3700 decreased, and a subtle peak at 2940 cm^{-1} sharpened (Figure S4, Supporting Information). This is consistent with the partial removal and reorganization of structural water.

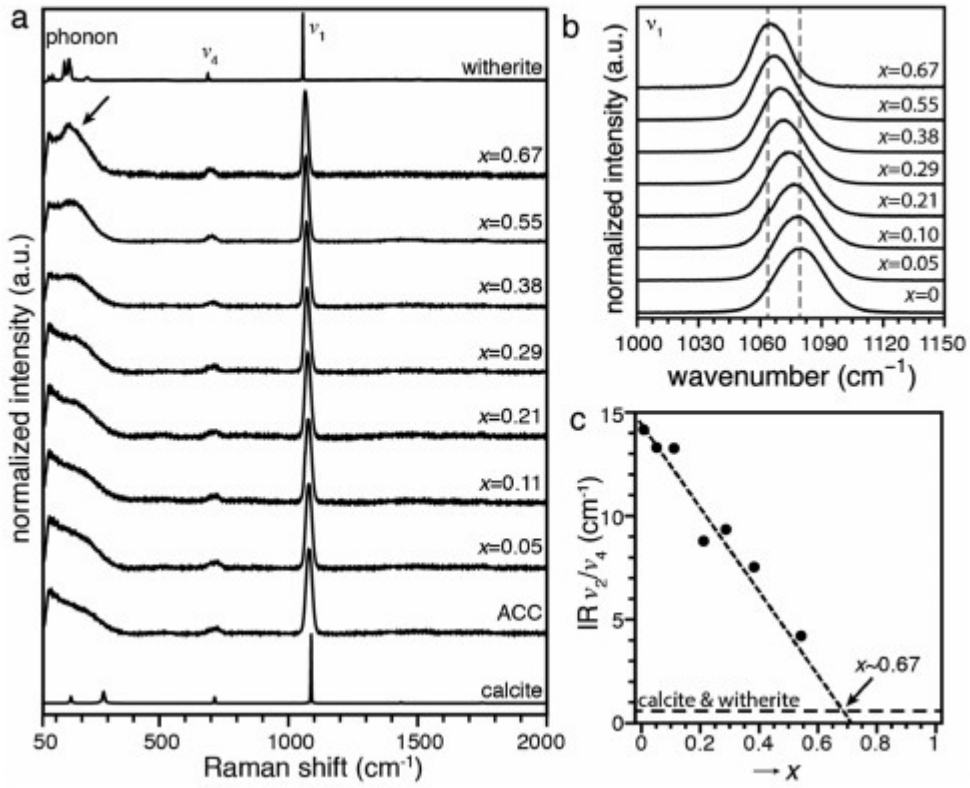

Figure 2

Raman spectra of ACC, ACBC and reference compounds calcite and witherite, showing the ν_1, ν_4, and lattice phonon (arrow) regions. For additional detail see Figures S3–S5 (Supporting Information). b) Raman ν_1 mode region, showing a shift in the peak center and decrease in FWHM with increasing barium. c) Plot of the ratio of intensities of the ν_2 and ν_4 modes in IR spectra vs. the barium cation mole fraction, x.

A broad feature below 300 cm^{-1}, commonly observed in ACC,[2] was also present in Raman spectra of ACBC. It shifted to lower wavenumbers with increasing barium content, increased in intensity, and sharpened, forming a broad but discernable peak centered at 145 cm^{-1} at x= 0.67 (Figure 2a). This peak coincided with the strongest acoustic phonon modes in witherite. Other witherite modes, especially the most intense (ν_1) at 1059 cm^{-1}, were absent. Drying ACBC with x = 0.41 at slightly elevated temperature and reduced pressure, as described above, did not impact the intensity of shape of this feature. It is therefore unlikely to be connected to structural water.

In addition to the behavior of individual modes, ratios of the intensity of IR internal mode peaks provide information about ordering in both amorphous and crystalline calcium carbonates.[5, 28, 29] In ACBC, the ν_2/ν_4 ratio decreased with increasing barium cation fraction, from 13.9 in ACC at x = 0, to 4.4 at x = 0.55 (Figure 2c), but remained higher than that of calcite (1.2) and witherite (1.0).

2.3 Modeling

Structural models for the ACBC phases were prepared using a combined molecular dynamics (MD) and density functional theory (DFT) approach. Supercells of 2 × 2 × 2 standard unit cells of calcite or aragonite were annealed using molecular dynamics at 10 000 K under NVT conditions (conservation of the number of ions, volume, and temperature), with an empirically fitted $CaCO_3$ potential.[30] Snapshots of the melt were gradually equilibrated to 298 K using MD, then fully relaxed using DFT (Figure 3 and Figures S6 and S7, Supporting Information). This process was repeated to generate six different ACC structures. We calculate the difference in enthalpies between the lowest-energy anhydrous ACC structures and calcite to be ΔH = 19–25 kJ mol^{-1} (Figure 3), in excellent agreement with experimental calorimetry measurements of ACC.[16, 24] The aqueous solubility for the lowest enthalpy ACC (described in detail in the Supporting Information) estimated only from ΔH is $K_{sp,ACC} = 10^{-5.3}$ M^2. The difference between the calculated K_{sp} from the experimentally measured $K_{sp,ACC}$ t $10^{-6.04}$–$10^{-7.5}$ M^2 (refs. 31-33) allows us to estimate a standard entropy of formation of ACC of approximately 21–40 J mol^{-1} K^{-1}.

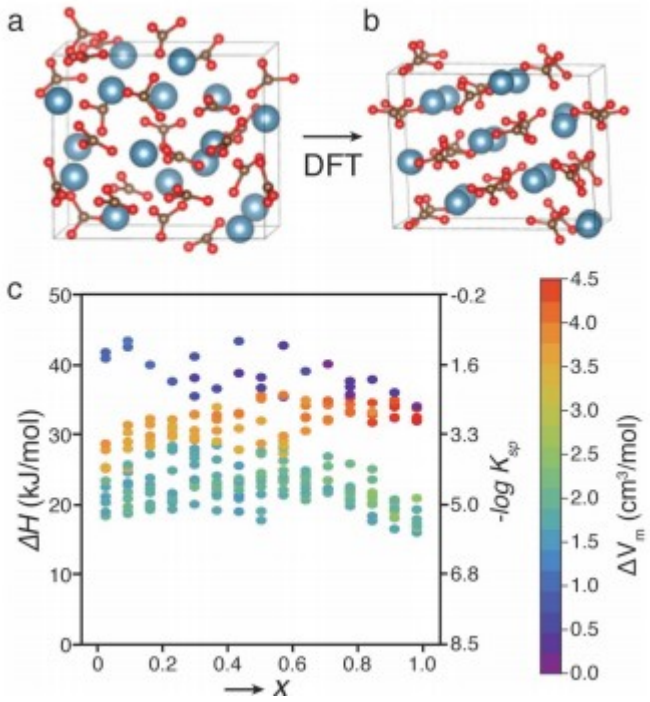

Figure 3

Example structures of a) MD generated and b) DFT-relaxed ACC. b) Plot of ΔH (left axis) and negative logarithm of the predicted solubility product (right axis) of DFT-relaxed ACBC structures against barium fraction x. Each marker corresponds to a fully relaxed structure; the marker color indicates the difference in molar volume (ΔV_m, cm^3 mol^{-1}) between the amorphous structure and an ideal orthorhombic-type $Ca_{(1-x)}Ba_xCO_3$ solid solution of the same composition. Note that structures fall into three horizontal bands with similar molar volume change (color).

ACBC was created by substituting Ba^{2+} for Ca^{2+} into ACC prior to the DFT-relaxation, giving an overall composition of $Ca_xBa_{1-x}CO_3$ in increments of Δx = 0.0625. Structurally, DFT relaxation coincided with a marked increase in

carbonate ordering. Specifically, the vector normal to the carbonate plane was essentially randomly oriented in space in MD-generated structures, while those in DFT-relaxed ACBC were mostly within ≈20° of one another (Figure S8, Supporting Information).

For all structures and across all compositions, the formation enthalpy ΔH was determined as the difference in enthalpy between ACBC and a phase-separated mixture of calcite ($CaCO_3$) and witherite ($BaCO_3$) at an equivalent overall composition. Solubility products for ACBC were determined in the same manner as those of ACC. The difference in molar volume, ΔV_m, between the V_m of the simulated structure and an ideal, aragonite/witherite-type $Ca_{1-x}Ba_xCO_3$ solid solution were calculated for each structure. Aragonite structure was chosen because it is the densest crystalline polymorph of $CaCO_3$, and because calcite-type $BaCO_3$has not been observed. In summary, ΔH tells us how much heat would be released by the transformation from ACBC to a mixture of pure calcite and witherite, and ΔV_m is the amount by which the molar volume decreases (density increases) if ACBC were to transform into a hypothetical aragonite structure with the same composition.

Inspection of a plot of ΔH and ΔV_m against the barium content (Figure 3c) revealed that the simulated ACBC structures fall into three distinct groups. While the lowest energy structures had an intermediate molar volume difference (ΔH = 19–25 kJ mol^{-1}, 1.0 < ΔV_m < 3.0 cm^3mol^{-1}), the highest energy structures had molar volume differences at the low end (ΔH = 35–45 kJ mol^{-1}, $\Delta V_m \cong 0.5$ cm^3 mol^{-1}), and the intermediate energy structures had molar volume differences at the high end (ΔH = 25–35 kJ mol^{-1}, $\Delta V_m > 3.0$ cm^3 mol^{-1}). Therefore, at any given composition the structures with the lowest energy do not have the highest density. This is also true for crystalline $CaCO_3$, emphasizing the importance of determining ΔH for benchmarking the simulations. In addition, the three groups could be distinguished by their average cation coordination number (Figure S9, Supporting Information), calculated by a Voronoi polyhedron method.[34] Strikingly, the structures with intermediate ΔH had the lowest average coordination number at any given composition. The low energy and high energy groups had similar average CNs. In all groups, the average CN increased with increasing barium content.

Given the stratification observed in the simulated structures, it made sense to consider the structures with low ΔH, consistent with literature values, and intermediate ΔV_m as representative of the lowest energy polyamorph. This allowed us to take a closer look at the distribution of the coordination numbers (CNs) for calcium and barium at each composition (Figure 4). The calcium CN decreased from 7.7 ± 0.7 (N = 64) at x = 0 to 7.1 ± 0.7 (N = 64) at x= 0.5, and remained at this value for higher barium contents. Unlike in reverse Monte Carlo fitting of experimental PDF data from ACC, where CNs as low as 3 were predicted,[35] we found that calcium appeared at least fivefold, but mostly sixfold and higher coordinated. The barium CN also decreased, from 9.8 ± 0.7 (N = 9) to 9.1 ± 0.8 (N = 64) at x = 0.5. Outside

the experimentally investigated range, the CN declined further to 8.3 ± 0.4 at $x = 1$ ($N = 80$). Even though the CNs for both cations individually decreased, the average CNs increased, from 7.7 ± 0.7 ($N = 64$) at $x = 0$ to 8.1 ± 1.3 ($N = 128$) at $x = 0.5$ and 8.3 ± 0.4 ($N = 80$) at $x = 1$, as the barium content increased (not shown).

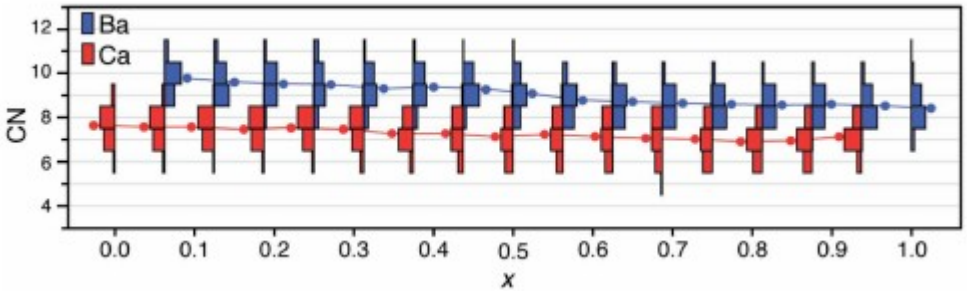

Figure 4

Histograms of the frequency at which coordination numbers for calcium ions (red bars) and barium ions (blue bars) occur in the lowest energy ACBC polyamorph (i.e., MD/DFT-simulated structures with ΔH = 19–25 kJ mol^{-1} and 1.0 < ΔV_m < 3.0 cm^3 mol^{-1}), as a function of barium content. The mean CN at each composition is indicated by a full circle and connected by lines as a guide to the eye.

2.4 X-Ray Absorption Spectroscopy

X-ray absorption spectra provide information about the symmetry in the first coordination shell of the probed cation, including average coordination number, lengths and average disorder of bonds, as well as order beyond the first coordination shell. X-ray absorption near-edge structure (XANES) spectra at the calcium K-edge exhibit a number of identifying features, including the sharp absorption edge, pre-edge peaks, white line peak above the edge, and postedge oscillations (Figure 5). The position of the edge is sensitive to the coordination number, for example, exhibiting a shift of 0.7 ± 0.1 eV toward higher energy relative to the calcite edge for each additional oxygen beyond the sixth.[5, 36] Consistent with this notion, the edge energy of reference materials calcite and barytocalcite ($Ba_{0.5}Ca_{0.5}CO_3$), both with sixfold calcium coordination, was identical within the experimental error (Table S4, Supporting Information). For ACBC with a barium fraction $x \leq 0.38$, the relative edge shift was nearly identical to that of ACC at 0.5 ± 0.1 eV, indicating an average coordination number of 6.8 ± 0.3 in the first shell. This is consistent with previous reports of ACC.[5, 37] At x= 0.55, the edge shift was slightly smaller, and the apparent coordination number dropped to 6.4 ± 0.2.

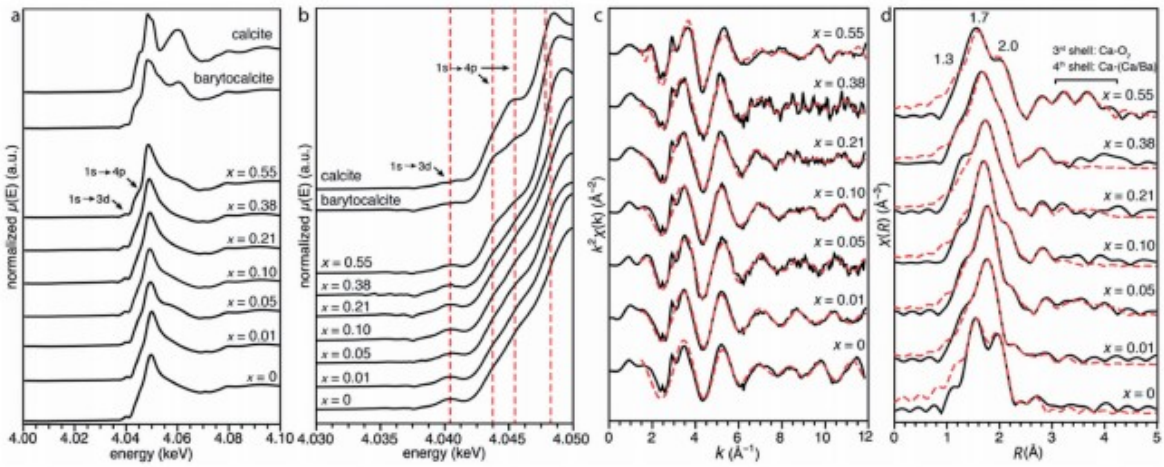

Figure 5

Calcium K-edge X-ray absorption spectroscopy of ACBC and reference compounds. a) XANES of calcite and barytocalcite reference materials, compared to ACBC with x = 0–0.55. b) Close up of the pre-edge features associated with a 1s → 3d transition (≈4.041 keV), a 1s → 4p transition (≈4.044 keV, 4.045 keV), and the absorption edge (≈4048.5 keV). c) k-space and d) R-space EXAFS experimental data (black line) and fitted curves (dashed red line).

Lowest in energy among the pre-edge features is the very weak 1s → 3d transition, ≈10 eV below the edge, which appears split in calcite and barytocalcite.[37] This feature is a singlet and is markedly more intense in ACC and ACBC (Figure 5b), indicating that the configuration of the first shell lacks an inversion center.[38] Two shoulders at slightly higher energy, ≈4 eV below the edge result from 1s → 4p transitions,[37] and are more pronounced in the crystalline reference compounds than in ACC and ACBC. While the position of the pre-edge features is largely independent of the barium content, the 1s → 3d transition decreased in intensity and became broader at x = 0.55. At the same time, the relative intensity of 1s → 4p transition at higher energy increased relative to that at lower energy. While the significance of this shift is unclear, the pre-edge region of ACBC (x = 0.55) qualitatively resembled that of barytocalcite and balcite (Figure 5a,b),[8] and may therefore be associated with the reduction in average coordination number towards six, and an associated increase in symmetry.

The postedge region of ACBC does not bear resemblance to either calcite nor barytocalcite, nor to that of aragonite, vaterite,[4] monohydrocalcite ($CaCO_3 \cdot H_2O$), and ikaite ($CaCO_3 \cdot 6H_2O$),[39, 40] but it has been shown to resemble that of balcite.[8] Because the balcite structure does not have well-defined crystallographic positions for carbonate oxygen, a structural model based on calcite, but with the coordination number in the first shell (Ca–O_1) fixed to the value determined by analysis of XANES spectra, was used to fit the extended X-ray absorption fine structure (EXAFS) spectra (Figure 5c,d). Varying the coordination number within the limits of the error did not produce a significant change in the quality of the fits (R-factor < 0.02). However, two separate bond distances were required for the fits to converge,

i.e., Ca–O_1 was split into Ca–$O_{1,1}$ and Ca–$O_{1,2}$. This is consistent with previously reported EXAFS spectra of ACC.[5]

Across all compositions, the distribution of oxygen between the Ca–O subshells evolved with increasing barium content (Table S4, Supporting Information) and resulted in changes in the peak intensities in *R*-space spectra at ≈1.4, 1.7, and 2.0 Å (Figure 5d). The most obvious effect of increasing barium content, however, was an increase in intensity of features associated with the third and fourth coordination shells (Ca–O_2 and Ca–(Ca/Ba)) at $x = 0.55$. Overlapping scattering contributions resulted in low sensitivity for differences between calcium and barium in the fourth shell, which had a roughly equal probability of occupancy at $x = 0.55$. However, it is clear that contributions from next-nearest neighbor cations in the fourth coordination shell emerged at this composition.

Near-edge spectra at the barium K-edge were qualitatively much more similar to each other than those at the calcium K-edge (Figure S10, Supporting Information). There were only two pronounced peaks of approximately equal intensity, the white line just above the edge at ≈37,450 eV, and another peak approximately 40 eV above the edge, but no pre-edge features. The lack of characteristic features in barium K-edge XANES spectra of crystalline carbonates, sulfates, and hydroxides has been attributed to relatively poor electron scattering compared to the absorber and low symmetry of the first few coordination shells.[41]

Barium K-edge EXAFS spectra of ACBC (Figure S10, Supporting Information) were fit with a structural model based on witherite (Table 1). The five inequivalent Ba-O distances in witherite were averaged to two to reduce the number of free parameters. Only the first (Ba–O) and second (Ba–C) shells were needed for accurate fitting (*R*-factor < 0.01). For all spectra, the coordination number was highly correlated with the Debye–Waller factor, and therefore the two were fit separately. Varying the coordination number within the calculated error did not change the fit quality appreciably. At all compositions, the coordination number of barium was significantly higher than that of calcium. At low barium content, the Ba coordination number was large (11–12), but its value decreased with increasing barium content. Note that the standard deviation associated with the coordination number is large (>1.0 for most compositions, Table 1), an indication of a broad distribution of coordination environments.

Table 1. Structure of the first coordination shell of Ca and Ba in ACBC determined by EXAFS.

x	CN[a]	Calcium K-edge						CN[b]	Barium K-edge						
		R [Å]			σ^2 [10^{-3} Å^2]				R [Å]			σ^2 [10^{-3} Å^2]		
		Ca–O_1	Ca–O_2	St. Dev.	Ca–O_1	Ca–O_2	St. Dev.		Ba–O_1	Ba–O_2	St. Dev.	Ba–O_1	Ba–O_2	St. Dev.
0	6.8 ± 0.3	2.21	2.40	0.010	2	2	1	–	–	–	–	–	–	–
0.01	6.8 ± 0.3	2.32	2.48	0.01	22	5	2	11 ± 1.0	2.62	2.79	0.14	19	13	20
0.05	6.8 ± 0.3	2.31	2.50	0.007	7	5	1	12 ± 0.7	2.75	2.78	0.02	10	23	3
0.10	6.8 ± 0.3	2.29	2.47	0.006	2	2	1	9.5 ± 1.1	2.76	2.89	0.04	11	16	7
0.21	6.8 ± 0.3	2.30	2.47	0.003	3	3	1	9 ± 1.6	2.70	2.81	0.01	7	13	3
0.38	6.8 ± 0.3	2.28	2.45	0.003	2	2	1	8 ± 1.2	2.71	2.83	0.01	9	10	1
0.55	6.4 ± 0.2	2.19	2.39	0.003	1	4	1	8 ± 1.0	2.69	2.84	0.01	7	9	1

[a]CN determined by edge energy shift from XANES; [b]CN determined by k-space EXAFS fitting.

2.5 PDF Analysis

Pair distribution function (PDF) analysis of X-ray total scattering data is a commonly used technique to study amorphous materials with no long-range order. Information about interatomic distances in real space can be obtained, and, with an appropriate structural model, can be assigned to specific atom-pair correlations.[35, 42] We performed PDF analysis of total X-ray scattering (Figure 6a) on ACC and ACBC between x = 0.05–0.55. The reduced structure factor $f(Q)$ was determined from the total scattering intensity $I(Q)$. Real-space information was then obtained by Fourier transformation of $f(Q)$. The resulting pair distribution function, $G(r)$, is the probability of finding an arbitrary pair of atoms separated by the distance r, and provides real space information about the interatomic distances on the ≈1–50 Å length scale. We further calculated the PDF for the simulated structures up to r = 8 Å (for example at x = 0.5, see Figure 6b).

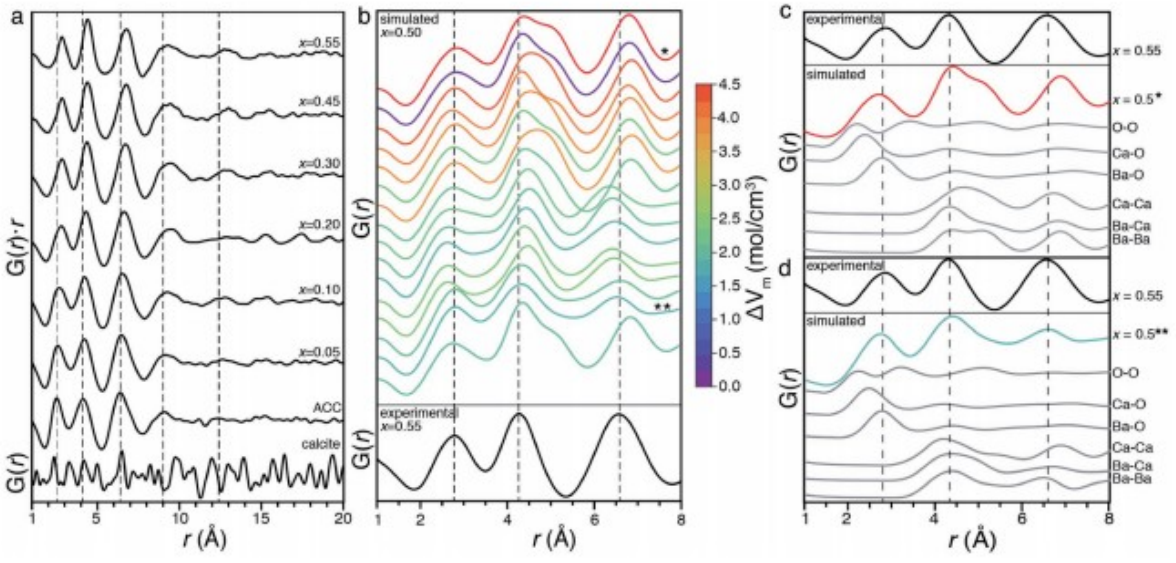

Figure 6

Analysis of experimental and simulated pair distribution functions (PDF). a) Plot of the experimental PDF for calcite, and of the r-weighted PDF for ACC and ACBCs, against the pair distance r. PDFs were

calculated from scattering data presented in Figure 1. b) A comparison of the experimental PDF of ACBC at $x = 0.55$ (black line) with PDFs calculated from simulated structures at $x = 0.50$. Simulated PDFs are stacked in order of ΔH, with the least stable structure (highest ΔH) at the top and the most stable structure at the bottom. PDFs are colored by ΔV_m. c,d) Plot of radial distribution functions for individual ion–ion pair correlation for two representative PDFs from (b), showing both high enthalpy (*) and low enthalpy (**) structures.

In calcite, sharp Bragg peaks are the dominant features in plots of the scattering intensity $I(Q)$ against the scattering vector Q (Figure 1a). Long-range crystalline order responsible for these Bragg peaks gives rise to sharp pair distance correlations well beyond $r = 50$ Å (Figure 6a). In contrast, the scattering pattern of ACC has characteristically broad features at $Q = 2.15$ and 3.08 $Å^{-1}$ (Figure 1a). Patterns of ACBC at low barium content strongly resemble that of ACC. With increasing x, a shoulder at $Q \approx 1.5$ $Å^{-1}$ and a peak at 4.7 $Å^{-1}$ increase in intensity and shift to lower Q, i.e., larger separation in real space.

Unlike the sharp pair correlations in calcite, the PDF of ACC is dominated by broad correlations at $r = 2.1$, 4.3, and 6.3 Å and a much broader feature at 8.9 Å. (Figure 6a; Figure S11, Supporting Information), consistent with prior results.[35, 37] Pair correlations in $G(r)$ of ACC break down after ≈10 Å, as previously observed for both ACC and ACMC.[16, 26, 37] Pair distribution functions for ACBC strongly resemble that of ACC, with four maxima at ≈2.5, 4.1, 6.3, and 8.9 Å. With increasing barium content, there was a systematic shift of these correlations to higher r. For example, the position of the maximum at 2.5 $Å^{-1}$ in ACC, which is primarily attributable to the Ca–O nearest-neighbor distance,[26, 37] increases continuously with x up to a value of 2.8 Å in ACBC at $x = 0.55$. The height of the maximum at ≈4.2 Å increases relative to that at 2.5 Å, and narrows subtly. A fifth, rather weak feature above 12.5 Å subtly becomes more pronounced with increasing barium content.

The experimental PDF is the sum of all two-species radial distribution functions (RDFs), weighted by the associated atomic X-ray scattering factors. While RDFs cannot be determined directly from experimental data, it is straighforward to extract them from simulated structural models (Figure 6b). The first major correlation in simulated RDFs at 2.5–2.8 Å, contains contributions from O–O pairs on the same carbonate anion, and Ca–O/Ba–O distances (i.e., the first coordination shell). These RDFs are relatively featureless beyond ≈4 Å and are similar between different simulated structures, and therefore do not contribute significantly to the PDFs beyond the first shell (Figure 6c). We find that correlations that extend beyond the first coordination shell, at 4.1–4.4 Å and 6.3–6.8 Å, are mostly associated with cation-cation (i.e., Ca–Ca, Ca–Ba, Ba–Ba) pairs.

Interestingly, we observe that the distance and magnitude of correlations are generally conserved between simulated polyamorphs from Figure 2. For example, at $x = 0.5$, higher energy structures with higher ΔV_m exhibit a split peak at 4.1–4.4 Å (Figure 6b), which the RDF indicates is due to two distinct Ba–Ba distances. The lower energy group of structures exhibits a Ba–Ba distance distribution. It should be noted that this relationship is not

completely deterministic, as the lowest energy simulated structure at $x = 0.5$ more closely resembled the highest energy structure than the group most similar in ΔV_m. However, at all compositions the groups of structures with similar ΔV_m and ΔH could generally be distinguished also by their PDFs.

3 Discussion

3.1 Synthesis and Amorphous Character

We have previously shown that hydrated amorphous calcium barium carbonate (ACBC, $Ca_{1-x}Ba_xCO_3 \cdot 1.2H_2O$) can be prepared by a variant of the low-temperature aqueous phase synthesis for amorphous calcium carbonate (ACC).[8, 43] In our hands, phase-pure ACBC could be isolated up to $x = 0.55$, but required short reaction times, rapid filtration and washing at low temperature. ACBC incorporated a significant fraction of barium cations present in the feed solution, on average ≈86 mol%. This is in sharp contrast to the ≈1% solubility limit of barium in calcite[44] and aragonite,[45] and of calcium in witherite.[46]Independent of the barium content, ACBC powders resembled ACC in that they were composed of partially aggregated, roughly spherical particles ≈100 nm in diameter (Figure 1). ACBC did not exhibit birefringence, and appeared amorphous by electron and X-ray diffraction. We note that these features are consistent with both a highly disordered material and an extremely fine grained structure with crystallite dimensions below 1 nm.[47]

3.2 Metastability

ACBC is metastable and converts to metastable “balcite” ($Ca_{1-x}Ba_xCO_3$ with Rm spacegroup) rather than stable calcite and witherite over a wide range of compositions (Figure 1). We have been unable to prepare phase pure ACBC at $x > 0.55$, at which point witherite is observed immediately after quenching.[8] Witherite increases in abundance relative to balcite with a nearly constant composition of $x \cong 0.5$ as the barium content increases (Figure 1; Table S1, Supporting Information), which may be due to the transient formation of a crystalline barium carbonate hydrate intermediate to witherite.[48] The disappearance of the calcite (113) peak between $x = 0$–0.25 suggests a gradual transition between calcite and balcite structures at low barium content. This may be similar to a second-order transition in high-temperature $Ca_{1-x}Ba_xCO_3$ that has been described previously.[46]

ACBC does not readily undergo phase transformation when kept dry, but crystallizes at elevated temperatures. Increasing barium content increased the temperature at which crystallization exotherms were first detected by DSC and DTA, from 290 °C at $x = 0$ to 335 °C at $x = 0.43$ (Figure S2, Supporting Information). In summary, barium acts to accelerate the transformation of ACC in aqueous solution, but retards transformation at elevated temperature. This behavior appears to be unique to barium, as large organic macromolecules have the opposite effect,[48] and magnesium,[16, 48] phosphate,[49] and sulfate[48] ions inhibit both aqueous

crystallization and crystallization at elevated temperature. A likely scenario is that the barrier to nucleation of balcite is lowered below those for calcite and witherite, and that higher barium content further lowers the barrier for balcite formation in the aqueous system. Slower crystallization at elevated temperature suggests that processes not mediated by solvent, e.g., solid state transformations, are inhibited by barium. Given the current focus on the structure and properties of ACBC, a quantitative analysis of the transformation kinetics of ACBC and the resulting balcite structures is beyond the scope of this report and will be detailed elsewhere.

It is clear that the composition of ACBC has a significant effect on its lifetime. We therefore set out to perform an in-depth analysis of ACBC structure as a function of the barium content. A comprehensive suite of techniques, including Raman and IR spectroscopy, X-ray absorption spectroscopy at both the calcium and barium K-edge, and pair distribution function analysis of X-ray total scattering data was employed. Atomic-scale simulations were used to determine thermodynamic properties of ACBC and relate them to atomic-scale structural motifs, and to extend the analysis to compositions that were not experimentally accessible. In order to do this, the role of structural water in ACBC was carefully considered.

3.3 The Role of Water in ACBC

Analysis of ACBC by TGA (x = 0–0.55, Figure S1, Supporting Information) revealed that the water content remained relatively constant at n = 1.2 ± 0.2 across all compositions. In this respect ACBC behaves similarly to amorphous magnesium carbonate (AMC, n = 1.3), ACMC (n = 1.3–1.5),[16, 50] and ACC ($n \cong 1.4$).[16, 25, 26, 50] The lack of a correlation between ionic radius of the cation and the water content is surprising, because the strength of dative water–metal bonds in the alkaline earth group decreases by a factor of two, and residence time of water decreases by over four orders of magnitude, going from Mg^{2+} to Ba^{2+}.[51-54]We would therefore expect to see a change in water content depending on the cation radius, for instance when comparing AMC and ACC. Further, we would expect the amount of water to depend on the mole fraction of magnesium in ACMC and of barium in ACBC. This is clearly not the case. As a consequence, there is no correlation between the water content of ACBC and the crystallization temperature, or its persistence at ambient temperature. Similarly, the crystallization enthalpy of synthetic ACC and ACMC does not correlate with water content.[16, 50] This indicates that the role of barium in ACBC, and of magnesium in ACMC, can be decoupled from that of water.

Biogenic ACCs, which may contain Mg^{2+}, PO_4^{2-}, and acidic proteins, exhibit different water content and crystallization enthalpies, and there is evidence that a hydrated form has longer life time than a dehydrated form.[24] Decreasing water content appears to correlate with a decreasing ν_2/ν_4 ratio in IR, an indication of increasing order that also corresponds to lower enthalpy structures.[24] However, the thermodynamic driving force for water

removal is the formation of a crystalline phase,[49] so it is unclear whether changing water content is the cause or effect of crystallization. Water is expected to have complex interactions with charged species in the solid state.[52] It appears to partially dissociate, and it may exhibit rapid dynamics.[25, 26, 35, 49, 55] There is evidence that it may be kinetically trapped during formation,[52, 56, 57] that it may be occluded in nanoscale pores,[25, 35] and that its distribution changes over the lifetime of amorphous precipitates.[25, 49] Perhaps most importantly, water can be removed from ACC with minimal change to the overall structure, as assessed by XAS and PDF.[26, 49]

Therefore, it is unclear how much water should be included in a simulated structure. As a consequence, we decided to exclude water from simulations altogether. While this approach has obvious limitations, it does provide significant detail about a very similar, and much less uncertain, approximation of the structure. If water does not have a significant effect on the thermodynamics of bulk ACBC, a great deal can be gleaned from the water-free model. Any discrepancies between experiments and water-free simulations may therefore highlight the most significant impacts that water has on the structure. This should be seen as a first step of a much more comprehensive approach that does include the water that is known to exist. However, inclusion of water would require much larger systems, and consideration of a much greater number of variables, and is therefore beyond the scope of this paper.

3.4 ACBC is a Solid Solution

Inspection of diffraction patterns (Figure 1a) confirms that none of the more stable crystalline phases, such as calcite, witherite, or balcite are present in ACBC. In addition, we do not find any indication for unmixing of ACBC into calcium and barium-rich amorphous phases. This is also clear from vibrational spectra, where the position of several internal modes of the carbonate ion (Raman: ν_1, $\nu_{4,1}$; IR: ν_3, ν_4) systematically shifted to lower wavenumber with increasing barium content (Figure 2; Figures S3–S5 and Table S2, Supporting Information). In case of unmixing, we would expect the spectra to be linear combinations of the pure compounds, and exhibit split or asymmetric peaks. Further support for homogenous distribution of calcium and barium ions comes from the continuous shift in bond lengths and coordination numbers in the first shell extracted from XAS (Figure 5; Figure S10 and Table S1, Supporting Information), which would be unaffected by the barium content if calcium and barium were not in molecular proximity. A microphase separation was postulated in the ACMC system, based on calorimetric data.[16] While the authors conclude that the PDFs of these materials neither support nor refute this observation, pair correlations from distinct and fixed Ca–O and Mg–O bond distances were observed over all compositions. The ratios of these correlations evolved with composition, which is consistent with local coordination environments around each cation that do not have a mutual impact on the other. In contrast, we did not

observe an equivalent trend for ACBC (Figure 6a, Figure S11, Supporting Information) within the resolution of our experiments (≈0.2 Å). Peaks at 2.1, 4.3, and 6.3 Å exhibited single maxima and shifted continuously to larger r with increasing barium. We therefore conclude that for $x \leq 0.55$, ACBC is indeed a solid solution, in which calcium and barium are homogeneously distributed.

3.5 Simulation of Anhydrous ACBC

As discussed in the preceding sections, we propose that simulating ACBC as an anhydrous solid solution is a reasonable first approximation. To accomplish this, a number of model structures were generated at each composition, using a two-step procedure in which an ACC structure was generated by MD, and ACC and ACBC structures were created from these by substitution and relaxation using DFT. The enthalpy of formation (ΔH = 19–25 kJ mol^{-1}) for the lowest energy ACC structures generated in this way showed excellent agreement to calorimetric data,[16, 24] providing confidence that the structures for which no thermochemical data is available are a reasonable approximation of the actual structure. Quite unexpectedly, we found that when MD-generated ACC and ACBC structures were relaxed using DFT, there was a distinct increase in the alignment of the carbonate ions (Figure S8, Supporting Information), but no obvious increase in cation lattice order. Orientational ordering upon the removal of water in MD-generated ACC has been suggested to produce vaterite-like local order.[58] An analysis of ΔH, estimated solubility product, difference in molar volume to a reference state (ΔV_m), and average coordination number revealed a stratification of the simulated structures consistent with the existence of three polyamorphs (Figure 2).

Overall, we find that simulations reproduce fairly well those structural features that we could probe experimentally. For example, the majority of PDFs of simulated structures grouped together as the lowest energy polyamorph closely resemble the experimental PDFs at similar composition (though this is not strictly true for all structures). Compare for example the PDFs of the simulated structures at x = 0.5 with the experimental PDF at 0.55 (Figure 6b). Lower energy structures had a single pair correlation at 4.1–4.4 Å, where higher energy structures exhibited a split peak due to multiple Ba–Ca correlations (apparent in the RDFs, Figure 6c). Lower energy structures also predicted the location of the pair correlation at 6.3–6.8 Å in the experimental PDF more accurately. Finally, the PDFs of simulated structures capture the systematic shifts with increasing barium content, which can be seen especially well for the pair correlation at 2.5–2.8 Å (Figure 6b). The close match between the PDFs of the lowest energy simulated structures and the experimental data inspires confidence that we can use the radial distribution functions (RDFs) that contribute to the simulated PDFs to identify the contributions of specific pairs of atoms to the experimental PDFs.

We further find that the bond distances and coordination numbers extracted from the lowest energy simulated structures (Figure 4; Figure S12, Supporting Information), and their dependence on the barium content, agreed well with trends observed in X-ray absorption spectroscopy (Table 1). For example, both the calcium and barium coordination numbers decrease between x = 0–0.5, with barium decreasing to a much greater extent (Figure 3, Table 1). Taken together, we find that despite the absence of water from the simulations, there is a fairly good match between predictions from the models and experimental data. We therefore feel confident that analysis of the simulated structures may provide valuable insights, especially where experimental data report average numbers, for instance coordination numbers, but simulations allow a more detailed analysis of coordination number distributions.

For amorphous carbonates synthesized previously that show extended life times when kept dry, ΔH decreases in magnitude with increasing cation radius.[9, 14-18] Consistent with this general trend, we find that ΔH for the lowest energy simulated amorphous barium carbonate structure (ABC, or ACBC with x = 1) is the lowest of any reported value at 16 kJ mol^{-1}. However, the difference in ΔH between AMC and ACC (≈19 kJ mol^{-1}) is much larger than that between ACC and ABC (≈3 kJ mol^{-1}), even though the difference in ionic radii is similar in both cases.[1] In mixed cation systems, experimental thermochemical data are only available for ACMC, where ΔH varies by as much as 25 kJ mol^{-1} with magnesium content.[16]In contrast, our simulations predict that ΔH of the lowest energy ACBC differs by less than 5 kJ mol^{-1} over the entire compositional range (Figure 3). Barium substitution therefore seems to carry minimal, if any, energy penalty. However, thermochemical experiments analogous to those performed on ACMC will be required to confirm this prediction.

Somewhat counterintuitively, the more soluble amorphous carbonates with higher ΔH have appear to be more persistent.[59] This means that despite the nominally higher supersaturation for ground state crystalline phases, nucleation and/or growth occur more slowly. Many amorphous carbonates of cations smaller than Ca^{2+}, including Mg^{2+}, Fe^{2+}, and Mn^{2+} have been synthesized as bulk powders,[9, 14-18] while those of larger cations such as Sr^{2+} and Ba^{2+} have not been observed in the absence of stabilizing additives[19-21] or confinement.[22] Consistent with this observation, ACBC at x = 0.5 is ≈18 kJ mol^{-1} above the ground state, yet transforms rapidly. At higher barium content, predicted ΔH values become even lower, and experimentally crystallization accelerates to the point where ACBC cannot be isolated in pure form. The magnitude of the effect is clearly not in proportion to the change in the predicted ΔH. Previously, we proposed that the rapid transformation of highly substituted ACBC may be due to nonclassical nucleation of balcite on or in ACBC, which is dependent on increasing structural similarity between ACBC and balcite.[8] We therefore performed a

careful analysis of local and mid-range structure in ACBC as a function of barium content.

3.6 Influence of Barium Content on Cation Coordination in the First Shell

We used XAS at the calcium and barium K-edges to investigate short range (<5 Å) order around both cations, and specifically the symmetry and distribution of bond lengths in the first coordination shell. The presence of the single 1s → 3d pre-edge feature at the calcium K-edge (Figure 5a,b) indicates that the first shell of calcium in ACBC, unlike that in calcite, is not centrosymmetric at any composition.[37] Consistent with this, both experiments (Figure 5, Table 1) and simulations (Figure 4) predict a significant fraction of calcium ions in sevenfold coordination, where centrosymmetry is impossible. At a CN of 8 and 6, centrosymmetry is in principle possible, but inspection of simulated structures indicates that the coordination geometry around most cations was irregular, with a range of bond distances (Figure S12, Supporting Information). Splitting of the first shell oxygen distance, required for convergence of EXAFS fitting, and large Debye-Waller factors with high uncertainty (Table 1) also support this notion. Taken together, simulations and EXAFS data both indicate that there is considerable disorder in the first coordination shell of calcium.

Based on the edge energy shift in XANES relative to calcite, calcium coordination in ACBC remains just below sevenfold up to $x = 0.38$, and drops to 6.4 at $x = 0.55$. While EXAFS is weighted toward shorter distances (smaller coordination number) due to inelastic photoelectron scattering and short core–hole lifetimes, the simulations have complete fidelity for more distant neighbors, and the coordination number for calcium determined from simulations (≈8) was slightly higher than those determined experimentally. Structural water may contribute to this difference. However, trends in the coordination number extracted from the lowest-energy simulated structures are in good agreement with the experimental data. Specifically, the most frequent coordination number for calcium in simulated ACC is 8 (48%, Figure 3), followed by 7 (36%) and 9 (7%), but with increasing barium content there is a reduction in the number of eight-coordinated calcium (to 30% at $x = 0.50$) and an increase in six-coordinated calcium (27%). Even though the Ba K-edge energy seems to be insensitive to the coordination number, fitting of EXAFS data revealed a pronounced shift, with a drop in average CN from 11–12 at low x to 8 at $x = 0.55$ (Table 1). Inspection of the simulated structures revealed the same trend toward lower CN with increasing barium content, and a significant increase of eightfold coordinated barium for $x \geq 0.5$ (Figure 4). This prediction is surprising, because barium is very rarely found in eightfold coordination in inorganic crystals, and we would therefore expect it would come with an energetic penalty. As discussed above, this does not seem to be the case.

In summary, barium coordination in ACBC is much more strongly impacted by barium content than that of calcium. While at low concentration barium

ions compete only with neighboring calcium ions for carbonate ligands, with increasing concentration, they will eventually start compete with each other, and as a consequence have to accept lower average CN. It seems likely that this competition will affect the chemical environment and bonding of carbonate ions in ACBC beyond the changes in bond length and stiffness that we expect when substituting barium for calcium.

3.7 The Carbonate Environment in ACBC

While the trigonal-planar geometry of carbonate anions is only subtly distorted in response to changes in the local chemical environment,[55] vibrational modes are quite sensitive differences in symmetry. We therefore analyzed Raman and IR spectra of ACBC as a function of barium content. In IR spectra, the ν_2 (out-of-plane bending) mode frequency and intensity is relatively invariant, while a reduction in the ν_4 (in-plane bending) mode intensity is observed with increasing local disorder.[29] The ratio of the integrated intensity of the ν_2 to the ν_4 mode (ν_2/ν_4) is used as an indicator of the width of the distribution of the Ca–O bond distance.[29] An increase in carbonate alignment has also been predicted to result in a decrease of the IR ν_2/ν_4 ratio in calcite,[60] suggesting that the coalignment of carbonates is correlated with the degree of local disorder. Significant reduction in ΔH upon DFT relaxation as a result of increasing carbonate alignment in simulated ACBC supports this notion.

In simulations of ACC, the ratio of IR ν_2/ν_4 mode intensities ranges from 3 for calcite to 10 as the Ca–O bond length distribution increases.[29] These values agree qualitatively with measurements of calcite and ACC.[29] We observed a decrease in the ν_2/ν_4 ratio from 13.9 in ACC to 4.4 at $x = 0.55$. This is indicative of a narrowing of the number of different chemical environments from the perspective of the carbonate ions, equivalent to an increase in order. Further support for an increase in order at high barium content comes from the observation that while the Raman ν_1 (symmetric stretch) mode was much broader in ACBC than in calcite or witherite, its full width at half maximum (FWHM) decreased as the barium content increased (Figure S4d, Supporting Information). With increasing barium content, the Raman ν_1 mode center shifted linearly from its position in ACC, close to that of calcite, towards lower wavenumbers near its position in witherite (Figures S3d and S4c,d, Supporting Information). The split ν_4 mode showed a qualitatively similar trend. However, while the $\nu_{4,1}$shift scaled with the barium content, the shift of the $\nu_{4,2}$ mode quickly reached a plateau at $x = 0.21$ (Figure S3c and S4a,b, Supporting Information). In addition, the $\nu_{4,2}$ mode increased in intensity relative to the $\nu_{4,1}$ mode. As a consequence, these modes increasingly resembled the ν_4 modes of aragonite-type carbonates (like witherite). In these materials three monodentate and three bidentate carbonates bind to each cation, with five separate oxygen distances, resulting in low-symmetry ν_4 modes that exhibit multiple peaks. Increasing coordination numbers in the first shell of both cations in EXAFS are

consistent with decreasing bidentate binding relative to monodentate binding (Supporting Information, Table S4–9).

3.8 Influence of Barium Content on Mid-Range Order

There are several indicators of increasing mid-range order with increasing barium content. The strong reduction of the IR ν_2/ν_4 ratio discussed in the previous section is one. Emergence of broad features with higher intensity in the lattice phonon mode region of Raman spectra is another (Figure 2a; Figure S3, Supporting Information). A number of sharp features corresponding to acoustic phonon modes below ≈300 cm^{-1} are frequently used to identify crystalline carbonates.[61-63] Low frequency phonon modes require positional ordering over at least one cation–cation distance (≈4–5 Å).[62] As scattering intensity scales with the fraction of ions oscillating in-phase, the increasing intensity of features below 300 cm^{-1}, and the emergence of even sharper peaks at ≈150 cm^{-1} at $x = 0.67$ (Figure 2a; Figure S3b, Supporting Information), are strong indications that there is increasing coherency in the collective vibrations of both cations and anions as the barium content increases. Partial drying does not affect these features (Figure S4e, Supporting Information), indicating that structural water us unlikely to be responsible.

An increase in order with increasing barium content was also apparent in EXAFS and PDF. Due to the rapid decay of signal with growing distance from the absorber in EXAFS, barium content had a rather subtle effect. At $x = 0.55$, an increase in the calcium K-edge *R*-space signal corresponding to the fourth shell (Ca-Ca/Ba, Figure 5) is indicative of increased positional ordering of cations within ≈5 Å. This is complemented by the decomposed RDFs, in which we observe an increase in the magnitude of correlations at 4.1–4.4 Å relative to that at 2.5–2.8 Å. An associated increasing correlation magnitude and narrower distribution of Ca–Ca, Ca–Ba, and Ba–Ba distances (Figure 6c) was observed in both experimental and simulated PDFs. Pair-correlations at 8.3 Å and 12.4 Å increased only subtly in experimental $G(r)$, placing an upper limit on the length scale of this ordering (Figure 6a), and suggesting that next-nearest-neighbor cation ordering is the dominant feature of ACBC order. Together, these observations confirm that order at mid-range length scales (5–15 Å) increases with increasing barium content. In this respect, ACBC is distinct from ACMC, where order appears to be limited to the first coordination shell.[16, 64] It is this mid-range order, on the length scale of critical nucleus sizes in carbonate systems,[65] that may contribute to structural similarity that promotes the formation of balcite.[8]

4 Conclusions

We find that substitution of up to 55 mol% of calcium with barium in ACC gives rise to ACBC that by all methods utilized appears amorphous. Simulations of anhydrous ACBC indicate that there exist as many as three polyamorphs of ACBC. Predictions based on structures associated with the lowest energy polyamorph matched experimental observations quite well,

and suggest that the decrease in lifetime of ACBC with increasing barium content is not due an decrease in formation enthalpy that would affect the thermodynamic driving force. Instead, ACBC short-range order evolved continuously, and mid-range order increased with increasing barium content. Specifically, cation–cation nearest neighbor ordering in ACBC emerged above a barium content of 50 mol%, and the ACBC local order becomes similar to that of balcite. This coincided with the composition at which the transformation to balcite becomes so rapid that it is no longer possible to prepare phase pure ACBC. Taken together, this provides support for the hypothesis that the presence of ACBC lowers the barrier to balcite nucleation selectively. A likely scenario is that ACBC acts as an increasingly powerful heterogeneous nucleator as the barium content increases. However, its retardation of crystallization at high temperatures suggests that this effect is mediated by the aqueous solution. These findings contribute significantly to an understanding of amorphous carbonate structures, their impact on thermodynamics, and a potential link to subsequent multistep transformation pathways. Such pathways may appear to be “non-classical” if the intermediate phase is too short-lived to be easily detected, for instance in the present system at very high barium content. Extending the structure–property relationships discovered for ACBC to other amorphous precursors may provide an appealing route to extend the design space of materials solid-solution compositions beyond thermodynamic solubility limits.

5 Experimental Section

Consumables: Unless otherwise noted, all aqueous solutions were prepared using ultra-pure water (ρ = 18.2 MΩ cm) prepared with a Barnstead NanoDiamond UF + UV purification unit. Reagent grade (>99%) $BaCl_2{\cdot}2H_2O$, $CaCl_2{\cdot}2H_2O$, $Na_2CO_3{\cdot}2H_2O$, $CaCO_3$, $BaCO_3$, (Sigma-Aldrich), and $(NH_4)_2CO_3$ (Fischer Scientific) were used without further purification. Iceland spar calcite was obtained from Dave's Down to Earth Rock Shop in Evanston, IL, USA. Geological reference materials witherite (cat #M21424) and barytocalcite (cat #M2145) were provided by the Field Museum of Natural History in Chicago, IL, USA.

ACBC Synthesis: Amorphous calcium barium carbonate was synthesized by rapid mixing of a cold aqueous solution of the alkaline earth chlorides ($[Ca^{2+}] + [Ba^{2+}] = 1$ M, pH 5.6–5.7, solution A) with a cold aqueous solution of Na_2CO_3 (1 M, pH 11.7, solution B). The mole fraction of Ba, x^{feed}, was varied between 0 and 1. For instance, to prepare solution A with $x^{feed} = 0.50$, 3.053 g $BaCl_2.2H_2O$ (12.5 mmol) and 1.838 g $CaCl_2.2H_2O$ (12.5 mmol) were dissolved in water to a final volume of 25 mL. For solution B, 3.100 g Na_2CO_3 (250 mmol) were dissolved in water to a final volume of 25 mL. Both solutions were then stored on ice for 2 h. Ice cold solution B was rapidly added to solution A, and the resulting solution mixed rapidly and thoroughly by vigorous shaking for 30 s. The resulting white precipitate was immediately collected by vacuum filtration through a 100 mm diameter Whatman no. 4 cellulose filter paper, washed three times with 5 mL cool

water (T = 10 °C), and dried under vacuum (R.T., $p \approx 10$ Pa = 10^{-1} Torr, 24 h). Unless otherwise noted, characterization was performed immediately thereafter.

Thermogravimetric Analysis: Thermogravimetric analysis (TGA) and differential thermal analysis (DTA) were performed simultaneously using a Mettler Toledo SDTA851. Analysis was performed on ACBC powders dried in vacuum for exactly 24 h after synthesis. Approximately 5 mg of the dry powder was held at 30 °C for 10 min to stabilize the sample environment, then heated to 1000 °C at a rate of 10 °C min^{-1} under dry N_2 flowing at a rate of 20 mL min^{-1}.

Weight change was tracked by the variable α, defined as

$$\alpha = \frac{w_0 - w_i}{w_0} = \frac{\Delta w}{w_0} \quad (1)$$

where w_0 is the initial weight and w_i is the instantaneous weight. The total fractional weight change, α_T, is the value of α at the final weight, $w_i = w_f$. Total fractional weight loss, Δa_T, is defined as 1-a_T. Fractional weight loss upon crystallization, Δa_c, is defined as $\alpha_{c1} - \alpha_{c2}$, where α_{c1} and α_{c2} are the values of α at temperatures corresponding to either side of the crystallization exotherm peak in differential scanning calorimetry, determined using the StarE v8.1 software package (Mettler Toledo). When multiple crystallization peaks were present, α_{c2} was chosen as the end of the final exothermic event. The molar water content, n, of the powders was calculated from

$$n = \frac{M_{H_2O}/\alpha_T}{(1-x)M_{Ca} + xM_{Ba} + M_C + 3M_O} \quad (2)$$

where M is the molecular mass of the subscripted species, the numerator is the molar fraction of water, the denominator is the molar fraction of $Ca_{1-x}Ba_xCO_3$, and x is the stoichiometric coefficient determined by XRF.

Differential Scanning Calorimetry: Differential scanning calorimetry and TGA were conducted in parallel on separate powder samples drawn from the same batch. Heat flow data in DSC was corroborated by simultaneous DTA (SDTA) performed during TGA runs (Figures S1 and S2, Supporting Information) and was in good qualitative agreement. Differential scanning calorimetry was performed on a Mettler Toledo DSC822e using the same approximate sample mass and N_2 flow rate as TGA, with the same heating schedule up to the instrument maximum of 500 °C. The crystallization temperature T_c was calculated from the onset of the crystallization exotherm in DSC curves determined with the StarE v8.1 software package.

X-ray Absorption Spectroscopy: Samples for X-ray absorption spectroscopy were synthesized in the same way as above, with drying times of at least 4 h under vacuum. Measurements were performed at the Dow-Northwestern-Dupont collaborative access team (DND-CAT), Sector 5-BM-D of the Advanced Photon Source at Argonne National Laboratory. Samples for

calcium K-edge measurements were spread on 8 μm Kapton tape and kept dry under a stream of He gas. For measurements performed at the barium K-edge, powders were loaded in quartz capillaries (0.5–1.5 mm outer diameter with 100 μm wall thickness). Larger diameter capillaries (1.5 mm) were used for samples synthesized at lower x (e.g., $x = 0.01$), while smaller capillaries (0.5 mm) were used at higher x (e.g. $x = 0.50$). Calibration at the calcium K-edge was performed with a geological Iceland spar (calcite) standard, for which the edge energy was set at 4038 eV. ACBC samples were measured relative to this value. Molybdenum foil (K-edge at 20.000 keV) was used to calibrate the barium K-edge to an absolute scale.

Data was analyzed using the Demeter package.[66] Normalization and background subtraction were carried out in Athena using Autobk. χ-data were weighted by k, k^2, and k^3between $1.6 < k < 11.5$ Å^{-1} for the calcium K-edge and between $2 < k < 14$ Å^{-1} for the barium K-edge. Fitting of the data to the crystal structures was performed using Artemis. The theoretical photoelectron scatting amplitudes and phase shifts were calculated using FEFF1. To generate the feff.inp file, which contains a list of the atomic coordinates centered at the absorbing atom, atoms[67] was used to calculate the atomic coordinates centered at calcium. The total theoretical $\chi(k)$ for each model was then constructed from the most important scattering paths and fit in R-space (calcium K-edge) or k-space (barium K-edge). Multiple scattering was not considered in amorphous materials. While maintaining sufficient number of degrees of freedom, as defined by the Nyquist criterion, the coordination number, bond distance, Debye–Waller factor, amplitude reduction factor, S_0^2 , and shift in energy origin, ΔE_0were allowed to float. S_0^2 and ΔE_0 were determined by simultaneously fitting all ACBC samples at either the calcium or barium K-edges. A total R-factor of 0.007 was obtained for simultaneous fitting of all six data sets for ACBC, with a reduced χ^2 of 558. Satisfactory fits were not obtained using S_0^2 from the crystalline reference samples, which for calcite and witherite were >1. Coordination numbers and Debye–Waller factors are highly correlated and were fit separately, but in each case with all other parameters floating. The validity of the fits was determined by the R-factor, which was minimized to ≤0.01. Complete fitting parameters are reported in the Supporting Information.

X-ray Total Scattering: X-ray total scattering was performed at the DND-CAT, Sector 5-BM-D of the Advanced Photon Source at Argonne National Laboratory. The X-ray energy (20.000 keV, $\lambda = 0.6195$ Å) was selected with a Si(111) monochromator, and calibrated with a molybdenum foil at the K-edge. Data were collected in Bragg-Brentano geometry with a Huber D8219 diffractometer ($2\theta = 4$–$169°$). The step size was 0.5° and the dwell time was 10 s. Four Si-drift solid state detectors with multichannel analyzers (MCA, ≈250 eV resolution at 20 keV) were used to simultaneously measure elastic scattering, calcium K-edge, and barium L-edge fluorescence. Total fluorescence signal was used for normalization of the elastic scattering.

Spectra were also normalized for incident beam intensity measured with an ion chamber ($p$$N_2$ = 73 kPa and pAr = 2 kPa). Scattering from the sample holder and Compton scattering were subtracted, and an absorption correction applied based on sample composition using GetPDFx2 software.[68]

Raman Microscopy: Approximately 5 mg of the dry powder was pressed onto a glass slide for Raman analysis. Raman spectra were obtained on a Horiba LabRam confocal Raman microscope with a laser of wavelength λ = 532 nm, operating at a power of 49 mW, and using a diffraction grating with 1800 g mm^{-1}, resulting in a final spectral resolution of 0.39 cm^{-1}. All spectra were recorded from individual precipitate particles using a 100× objective lens in air (0.9 NA, minimum resolution ≈361 nm). Mode centers, relative intensities, and full peak width at half maximal intensity (FWHM) were determined by fitting one or more Gaussians to the spectral region of interest. Fitting was performed manually using in-house code written in Mathematica.

Fourier Transform Infrared (FTIR) Spectroscopy: Immediately following Raman microscopy, ≈8 mg of the dry powder was mixed with ≈160 mg KBr in a mortar and pestle. Approximately 25 mg of the mixture was then pressed into a pellet at 7 MPa. Bulk FTIR spectra from KBr pellets containing ≈5.0 wt% ACBC powder were acquired in the range from 400 to 4000 cm^{-1}on a Thermo Nicolet Nexuz 870 FT-IR in transmission geometry, with a spectral resolution of 4 cm^{-1}.

MD/DFT: Amorphous $CaCO_3$-$BaCO_3$ solid-solutions were prepared from supercells of the rhombohedral and orthorhombic carbonate structures. The rhombohedral supercell was constructed from a 2 × 2 × 2 primitive calcite unit cell (16 formula units), the orthorhombic unit cell from a 2 × 2 × 1 conventional cragonite unit cell (16 formula units). The amorphous structure was prepared by annealing the pristine calcium carbonate structures in LAMMPS[69] under NPT conditions at 10000 K, using an empirically fitted $CaCO_3$ potential.[30]Snapshots of the melt were then quenched and equilibrated at 298 K. Finally, the amorphous unit cell was relaxed in DFT at T = 0 K with full ionic and unit-cell relaxations.

DFT calculations were performed using the Vienna Ab-Initio Software Package (VASP),[70]using the projector augmented wave (PAW)[71] method with the Perdew–Burke–Erzhenhoff (PBE)[72] generalized-gradient approximation. Plane-wave basis cutoff energies were set at 520 eV for all calculations. Brillouin zones were sampled using Gaussian smearing, with at least 1000 k-points per reciprocal atom. Atoms were initially relaxed until energy differences between ionic steps were 1 meV per atom. All structure preparations were performed using the Python Materials Genomic (Pymatgen) package.[73]

ACBC structural models generated in this way are not truly amorphous, but are rather periodic approximants, with lattices that satisfy periodic boundary conditions. Periodic approximants all have dimensions of at least 12 Å × 12 Å

× 12 Å, so the long-range interactions of the lattice are only minor contributions to the total energy of the structure, allowing our periodic approximants to be reasonable models for the energetics and local structure of the amorphous $Ca_{1-x}Ba_xCO_3$ phase.

Solid-solution supercells were initialized by substituting Ba^{2+} onto the Ca^{2+} sites, and rescaling the molar volume of the supercell by Vegard's law.[74] A modified Ewald summation was used to bias solid solutions towards structures with maximized Ba^{2+}–Ba^{2+} interatomic distances under periodic boundary conditions. Total energies of the supercells were calculated in DFT, with full ionic and unit-cell relaxations. Coordination analyses were performed using a weighted Voronoi coordination method,[34] as found in the structure analyzer package of Pymatgen. We used a larger Voronoi cutoff radius for Ba (3.48 Å) than for Ca (3.0 Å). Molar volumes of ACBC were compared to an ideal aragonite-type solid solution, calculated by extrapolation between aragonite and witherite, also using Vegard's law.

Computed radial distribution functions (RDFs) were calculated using a kernel density estimate of the two-species pair-correlations in the crystal structure under periodic boundary conditions. The radial distributions for each pair of species, $G_{ij}(r)$, were summed to form the pair-distribution function by the equation

$$G(r) = \sum_{i,j} w_{i,j} G_{i,j}(r) \quad (3)$$

where the weighting factor w_{ij} depends on the concentration and scattering power $f(q)$ of the atomic species by

$$w_{i,j} = \frac{c_i c_j f_i(q) f_j(q)}{\left[\sum c_i f_i(q)\right]^2} \quad (4)$$

For this work, w_{ij} was evaluated for $q = 0$.

Acknowledgements

This work was supported in part by the International Institute for Nanotechnology, NSF (DMR-1508399), and ARO (W911NF-16-1-0262). In situ-WAXS, EXAFS, and hr-PXRD were performed at the DuPont-Northwestern-Dow Collaborative Access Team (DND-CAT) located at Sector 5 of the Advanced Photon Source (APS) a U.S. Department of Energy (DOE) Office of Science User Facility operated for the DOE Office of Science by Argonne National Laboratory under Contract No. DE-AC02-06CH11357. The authors thank Drs. Steven Weigand, Qing Ma, and Denis Keane. WS, SJ, and GC were supported by the U.S. DOE, Office of Science, Basic Energy Sciences, under contract no. UGA-0-41029-16/ER392000 as part of the DOE Energy Frontier Research Center “Center for Next Generation of Materials by Design: Incorporating Metastability.” We used computing resources at Center for Functional Nanomaterials, which is a U.S. DOE Office of Science Facility at Brookhaven National Laboratory, under contract no. DE-SC0012704. The

references of this manuscript were updated on January 10, 2018, after initial publication in early view, to correct the reference list from ref.46 and onwards.

References

[1] A. V. Radha, A. Navrotsky, Rev. Mineral. Geochem. 2013, 77, 73. [2] L. Addadi, S. Raz, S. Weiner, Adv. Mater. 2003, 15, 959. [3] A. Gal, K. Kahil, N. Vidavsky, R. T. DeVol, P. U. P. A. Gilbert, P. Fratzl, S. Weiner, L. Addadi, Adv. Funct. Mater. 2014, 24, 5420. [4] D. Gebauer, P. N. Gunawidjaja, J. Y. P. Ko, Z. Bacsik, B. Aziz, L. Liu, Y. Hu, L. Bergström, C.-W. Tai, T.-K. Sham, M. Edén, N. Hedin, Angew. Chem., Int. Ed. 2010, 49, 8889. [5] Y. Politi, Y. Levi-Kalisman, S. Raz, F. Wilt, L. Addadi, S. Weiner, I. Sagi, Adv. Funct. Mater. 2006, 16, 1289. [6] C. Rodriguez-Navarro, K. Kudłacz, Ö. Cizer, E. Ruiz-Agudo, CrystEngComm 2016, 17, 58. [7] J. H. E. Cartwright, A. G. Checa, J. D. Gale, D. Gebauer, C. I. Sainz-Díaz, Angew. Chem., Int. Ed. 2012, 51, 11960. [8] M. L. Whittaker, D. Joester, Adv. Mater. 2017, 6, 1606730. [9] S. A. Kondrat, P. J. Smith, P. P. Wells, P. A. Chater, J. H. Carter, D. J. Morgan, E. M. Fiordaliso, J. B. Wagner, T. E. Davies, L. Lu, J. K. Bartley, S. H. Taylor, M. S. Spencer, C. J. Kiely, G. J. Kelly, C. W. Park, M. J. Rosseinsky, G. J. Hutchings, Nature 2016, 531, 83. [10] L. Bloch, Y. Kauffmann, B. Pokroy, Cryst. Growth Des. 2014, 14, 3983. [11] I. Saika-Voivod, P. H. Poole, F. Sciortino, Nature 2001, 412, 1. [12] O. Mishima, Y. Suzuki, Nature 2002, 419, 597. [13] H. W. Sheng, H. Z. Liu, Y. Q. Cheng, J. Wen, P. L. Lee, W. K. Luo, S. D. Shastri, E. Ma, Nat. Mater. 2007, 6, 192. [14] T. Z. Forbes, A. V. Radha, A. Navrotsky, Geochim. Cosmochim. Acta 2011, 75, 7893. [15] O. Sel, A. V. Radha, K. Dideriksen, A. Navrotsky, Geochim. Cosmochim. Acta 2012, 87, 61. [16] A. V. Radha, A. Fernandez-Martinez, Y. Hu, Y.-S. Jun, G. A. Waychunas, A. Navrotsky, Geochim. Cosmochim. Acta 2012, 90, 83. [17] A. V. Radha, A. Navrotsky, Am. Mineral. 2014, 99, 1063. [18] A. V. Radha, A. Navrotsky, Cryst. Growth Des. 2015, 15, 70. [19] S. J. Homeijer, R. A. Barrett, L. B. Gower, Cryst. Growth Des. 2010, 10, 1040. [20] S. Matsunuma, H. Kagi, K. Komatsu, K. Maruyama, T. Yoshino, Cryst. Growth Des. 2014, 14, 5344. [21] J. L. Littlewood, S. Shaw, C. L. Peacock, P. Bots, D. Trivedi, I. T. Burke, Cryst. Growth Des. 2017, 17, 1214. [22] S. E. Wolf, L. Müller, R. Barrea, C. J. Kampf, J. Leiterer, U. Panne, T. Hoffmann, F. Emmerling, W. Tremel, Nanoscale 2011, 3, 1158. [23] A. V. Matyskin, B. Ebin, M. Tyumentsev, S. Allard, G. Skarnemark, H. Ramebäck, C. Ekberg, J. Radioanal. Nucl. Chem. 2016, 1. [24] A. V. Radha, T. Z. Forbes, C. E. Killian, P. U. P. A. Gilbert, A. Navrotsky, Proc. Natl. Acad. Sci. USA 2010, 107, 16438. [25] J. Ihli, W. C. Wong, E. H. Noel, Y.-Y. Kim, A. N. Kulak, H. K. Christenson, M. J. Duer, F. C. Meldrum, Nat. Commun. 2014, 5, 1. [26] M. P. Schmidt, A. J. Ilott, B. L. Phillips, R. J. Reeder, Cryst. Growth Des. 2014, 14, 938. [27] W. Sun, S. T. Dacek, S. P. Ong, G. Hautier, A. Jain, W. D. Richards, A. C. Gamst, K. A. Persson, G. Ceder, Sci. Rep. 2016, 2, 1600225. [28] E. Beniash, J. Aizenberg, L. Addadi, S. Weiner, Proc. R. Soc. London, B 1997, 264, 461. [29] R. Gueta, A. Natan, L. Addadi, S. Weiner, K. Refson, L. Kronik, Angew. Chem., Int. Ed. 2007, 46, 291. [30] P.

Raiteri, J. D. Gale, D. Quigley, P. M. Rodger, J. Phys. Chem. C 2010, 114, 5997. [31] L. Brecevic, A. E. Nielsen, J Cryst. Growth 1989, 98, 504. [32] D. Gebauer, H. Cölfen, Nano Today 2011, 6, 564. [33] J. R. Clarkson, T. J. Price, C. J. Adams, Faraday Trans. 1992, 88, 243. [34] M. OKeeffe, Acta Crystallogr. 1979, A35, 772. 35] A. L. Goodwin, F. M. Michel, B. L. Phillips, D. A. Keen, M. T. Dove, R. J. Reeder, Chem. Mater. 2010, 22, 3197. [36] F. E. Sowrey, L. J. Skipper, D. M. Pickup, K. O. Drake, Z. Lin, M. E. Smith, R. J. Newport, Phys. Chem. Chem. Phys. 2004, 6, 188. [37] F. M. Michel, J. MacDonald, J. Feng, B. L. Phillips, L. Ehm, C. Tarabrella, J. B. Parise, R. J. Reeder, Chem. Mater. 2008, 20, 4720. [38] J. L. Fulton, S. M. Heald, Y. S. Badyal, J. M. Simonson, J. Phys. Chem. A 2003, 107, 4688. [39] Y. Levi-Kalisman, S. Raz, S. Weiner, L. Addadi, I. Sagi, Adv. Funct. Mater. 2002, 12, 43. [40] I. P. Swainson, Am. Mineral. 2008, 93, 1014. [41] A. A. Finch, N. Allison, H. Steaggles, C. V. Wood, J. F. W. Mosselmans, Chem. Geol. 2010, 270, 179. [42] R. J. Reeder, Y. Tang, M. P. Schmidt, L. M. Kubista, D. F. Cowan, B. L. Phillips, Cryst. Growth Des. 2013, 13, 1905. [43] N. Koga, Y. Nakagoe, H. Tanaka, Thermochim. Acta 1998, 318, 239. [44] A. Tesoriero, J. Pankow, Geochim. Cosmochim. Acta 1996, 60, 1053. [45] M. Dietzel, N. Gussone, A. Eisenhauer, Chem. Geol. 2004, 203, 139. [46] L. L. Chang, J. Geol. 1965, 73, 346. [47] P. Rez, S. Sinha, A. Gal, J. Appl. Crystallogr. 2014, 47, 1651. [48] M. Whittaker, P. J. M. Smeets, H. Asayesh-Ardakani, R. Shahbazian-Yassar, D. Joester, Angew. Chem. Int. Ed. 2017, 129, 16244. [49] J. Ihli, Y.-Y. Kim, E. H. Noel, F. C. Meldrum, Adv. Funct. Mater. 2012, 23, 1575. [50] S. Kababya, A. Gal, K. Kahil, S. Weiner, L. Addadi, A. Schmidt, J. Am. Chem. Soc. 2015, 137, 990. [51] C. R. Blue, P. M. Dove, Geochim. Cosmochim. Acta 2015, 148, 23. [52] L. N. Plummer, E. Bunsenberg, Geochi 1982, 46, 1011. [53] J. R. Dorvee, A. Veis, J. Struct. Biol. 2013, 183, 278. [54] M. I. Chaudhari, M. Soniat, S. B. Rempe, J. Phys. Chem. B 2015, 119, 8746. [55] P. Raiteri, R. Demichelis, J. D. Gale, J. Phys. Chem. C 2015, 119, 24447. [56] S. Sen, D. C. Kaseman, B. Colas, D. E. Jacob, S. M. Clark, Phys. Chem. Chem. Phys. 2016, 18, 20330. [57] A. F. Wallace, L. O. Hedges, A. Fernandez-Martinez, P. Raiteri, J. D. Gale, G. A. Waychunas, S. Whitelam, J. F. Banfield, J. J. De Yoreo, Science 2013, 341, 885. [58] R. Demichelis, P. Raiteri, J. D. Gale, D. Quigley, D. Gebauer, Nat. Commun. 2011, 2, 590. [59] M. Saharay, R. James Kirkpatrick, Chem. Phys. Lett. 2014, 591, 287. [60] C. C. Tester, M. L. Whittaker, D. Joester, Chem. Commun. 2014, 50, 5619. [61] S. Sinha, P. Rez, Mater. Chem. Phys. 2015, 157, 56. [62] C. Carteret, A. Dandeu, S. Moussaoui, H. Muhr, B. Humbert, E. Plasari, Cryst. Growth Des. 2009, 9, 807. [63] L. Valenzano, Y. Noël, R. Orlando, C. M. Zicovich-Wilson, M. Ferrero, R. Dovesi, Theor. Chem. Acc. 2007, 117, 991. [64] M. Prencipe, F. Pascale, C. M. Zicovich-Wilson, V. R. Saunders, R. Orlando, R. Dovesi, Phys. Chem. Miner. 2004, 31, 559. [65] G. Cobourne, G. Mountjoy, J. D. Rodriguez-Blanco, L. G. Benning, A. C. Hannon, J. R. Plaisier, J. Non-Cryst. Solids 2014, 401, 154. [66] Q. Hu, M. H. Nielsen, C. L. Freeman, L. M. Hamm, J. Tao, J. R. I. Lee, T. Y. J. Han, U. Becker, J. H. Harding, P. M. Dove, J. J. De Yoreo, Faraday Disc. 2012, 159, 509. [67] B. Ravel, M. Newville, J. Synchrotron Radiat. 2005, 12, 537. [68] B. Ravel, J. Synchrotron Radiat.

2001, 314. [69] X. Qiu, J. W. Thompson, S. J. L. Billinge, J. Appl. Crystallogr. 2004, 37, 678. [70] S. Plimpton, J. Comput. Phys. 1995, 117, 1. [71] G. Kresse, J. Furthmüller, Phys. Rev. B 1996, 64, 11169. [72] G. Kresse, D. Joubert, Phys. Rev. B 1995, 59, 1758. [73] J. P. Perdew, K. Burke, M. Ernzerhof, Phys. Rev. Lett. 1996, 77, 3865. [74] S. P. Ong, W. D. Richards, A. Jain, G. Hautier, M. Kocher, S. Cholia, D. Gunter, V. L. Chevrier, K. A. Persson, G. Ceder, Comput. Mater. Sci. 2013, 68, 314. [75] A. R. Denton, N. W. Ashcroft, Phys. Rev. A 1991, 43, 3161.